# Chip-Scale Terahertz Carbonyl Sulfide Clock: An Overview and Recent Studies on Long-Term Frequency Stability of OCS Transitions

Mina Kim, *Student Member, IEEE*, Cheng Wang, *Student Member, IEEE*, Zhi Hu, *Student Member, IEEE*, and Ruonan Han, *Member, IEEE*

*(Invited Paper)*

***Abstract*—This paper reviews the recent innovations of a miniature time-keeping device with high affordability: chip-scale molecular clock. It is based on the recent research progress of high-precision terahertz (THz) rotational spectrometers, especially those using CMOS integrated circuit technologies. The clock probes the rotational modes of carbonyl sulfide ($^{16}$O$^{12}$C$^{32}$S) molecule gas and then calibrates its MHz output according to the measured terahertz transition frequency of OCS. In contrast to cesium/rubidium atomic clocks, the THz OCS clock has fully electronic operations and, hence, a significantly simplified implementation. In particular, it is realizable on a waveguide-attached CMOS chip, which minimizes the form factor and cost. Based on a lab scale prototype with an Allan deviation in the $10^{-11}$ range, this paper for the first time studies two critical metrics related to the long-term stability of THz OCS clocks. These metrics are the clock sensitivities to temperature change of the OCS gas and external magnetic field. The measured average temperature coefficient of the clock, without ovenized temperature stabilization and temperature compensation, is $9.5 \times 10^{-11}$/°C in the range of 28 °C–70 °C. Next, the measured clock shift in response to a 75 G external magnetic field is $<4 \times 10^{-11}$, with a theoretical value near $10^{-13}$. Lastly, this paper also reviews the first reported CMOS prototype of the clock, which consumes only 66 mW dc power and achieves an Allan deviation of $3.8 \times 10^{-10}$ ($\tau = 1000$ s). Approaches for performance improvements and potential monolithic chip implementation are discussed. These studies present the feasibility of a CMOS-based magnetic-shield/heater-free clock with high energy efficiency and sub-*ppb* stability over a wide range of operation condition.**

***Index Terms*—Carbonyl sulfide (OCS), CMOS, frequency stability, molecular clock, rotational spectroscopy, temperature coefficient, Zeeman.**

## I. Introduction

An ELECTROMAGNETIC wave, when illuminating on a polar molecule in gaseous phase, exerts a torque on the dipole moment of the molecule. When the photon energy of the wave matches the difference between two adjacent quantized rotational energy levels, rotational transitions are excited [1]. Those transitions normally occur at microwave to terahertz (THz[1]) frequencies, and the related spectroscopic instruments are used for molecular identifications. Note that for lightweight molecules, the rotational lines normally lie within the THz regime. And even for other heavier molecules, the intensity of the lines is significantly larger (hence, higher signal-to-noise ratio, SNR) in THz than in microwave regime (see more details in Section III). This is why the THz frequency range is preferred for rotational spectroscopy, albeit the long-standing challenges in the construction of THz hardware.

In the past, THz spectrometers had most of their applications in astronomy, for the analysis of interstellar matters [2]. Recent research showed that continuous wave, electronic THz spectrometers also enabled portable gas sensing with ultrawide detection range and absolute specificity [3], [4]. With the assistance of a gas preconcentrator, the demonstrated sensitivity reaches sub-part-per-trillion (*ppt*) level [4]. These features make the spectrometer highly attractive for pollution monitoring, breath analysis, and hazard detection [5], [6]. With the ever-increasing speed of CMOS/SiGe transistors, small-size and low-cost rotational spectrometers operating in low-THz range (200–500 GHz) have become possible. Silicon-chip prototypes reported by the University of Texas [7], [8], IHP Microelectronics [9], [10], and MIT [11]–[13] have delivered electronic performance similar to that of compound-semiconductor multiplier systems; sensing of gas mixtures with high sensitivity and specificity has been demonstrated.

Interestingly, in the low-THz regime, the Doppler-limited linewidth of molecular rotational resonance is at megahertz (MHz) or below [4], [13], which provides a set of highly stable frequency references with a quality factor close to $10^6$.

Manuscript received March 9, 2019; accepted April 3, 2019. Date of publication May 22, 2019; date of current version July 1, 2019. This work was supported in part by National Science Foundation under Grant CAREER ECCS-1653100 and Grant ECCS-1809917, in part by MIT Lincoln Laboratory under Grant ACC-672, and in part by the fellowships from Texas Instruments and Kwanjeong Scholarship for Graduate Study. *(Corresponding author: Ruonan Han.)*

The authors are with the Department of Electrical Engineering and Computer Science, Massachusetts Institute of Technology, Cambridge, MA 02139 USA (e-mail: minahkim@mit.edu; wangch87@mit.edu; zhihu@mit.edu; ruonan@mit.edu).

Color versions of one or more of the figures in this paper are available online at http://ieeexplore.ieee.org.

Digital Object Identifier 10.1109/TTHZ.2019.2918436

[1]In this paper, we adopt the relaxed definition of THz as the frequency range between 0.1–10 THz.

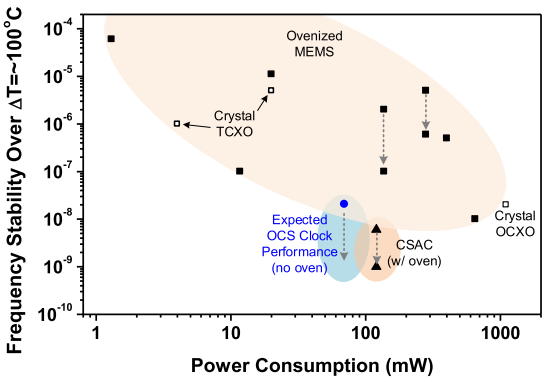


Fig. 1. Expected OCS THz clock performance, in comparison with other miniature frequency references (including ovenized MEMS oscillators [17]–[23], crystal TCXO [24], [25], crystal OCXO [26], and CSAC [27]). OCS clocks with improved gas cell design are expected to deliver better stability than the value shown here. The dash line arrows indicate the stability improvement with temperature-compensation algorithm.

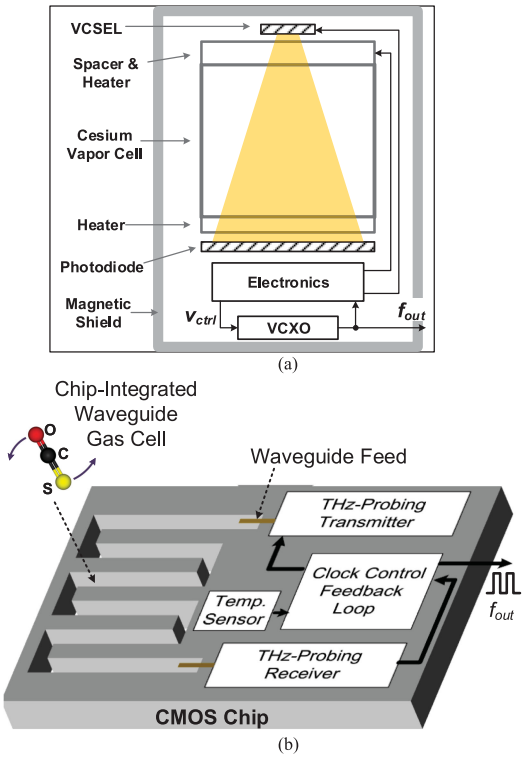


Fig. 2. (a) Structure of current CSACs. (b) Prospective single-chip implementation of a THz molecular clock (see Section V-A).

Therefore, it is possible to implement an ultrasmall, low-cost "molecular clock" using a CMOS spectrometer inside a closed feedback control loop [14]. Such miniature frequency references are critical for new generations of navigation, sensing, and communication systems, especially when the GPS timing service is unreliable or even completely unavailable.

For example, in undersea oil explorations using reflection seismology, a large array of battery-powered hydrophone sensors is deployed to detect the precise time-of-arrival of a sonar wave reflected by the oil buried in the seabed [15]. For accurate mapping of the oil location, the timing error of each hydrophone sensor should be within 1–10 ms across the entire deployment duration of up to one year. The required timing stability, on the order of $10^{-10}$–$10^{-11}$, solely relies on the local clocks due to the unavailability of GPS signal under the sea. Another example application comes from the evolution of wireless networking. In 4G networks, the phase/time synchronization error among adjacent base stations should be within a few $\mu$s; in comparison, the new 5G standard with ultrahigh data traffics and connection densities tightens the above-mentioned requirement to $\sim$100 ns for carrier aggregation and even to $\sim$10 ns for high-accuracy positioning [16]. A large number of high-stability clocks are, therefore, required for the timing holdover in complementary to GPS receivers (in case of the GPS reception failure) and to synchronize fiber networks.

At present, the most common miniature references are based on crystal/MEMS oscillators, which have low cost but are highly sensitive to environmental changes (e.g., temperature) [17]–[22], [24], [25]. The output drift over $\sim$100 K temperature range is normally in the realm of part-per-million (*ppm*), when back-end temperature compensation is applied (see Fig. 1). Ovenized temperature stabilization improves the stability to tens of part-per-billion (*ppb*), but is at the expense of high-power consumption (a few hundreds of milliwatts to a few watts) [23], [26]. In comparison, atomic clocks, which lock their outputs to atomic spin transitions, provide superior stability up to $10^{-18}$ [28], but in the meantime require hardware constructions that are impractically large and costly for many mainstream electronic systems [29]. For example, advanced atomic fountain clocks use laser cooling and meter-height tossing of atom cloud to achieve long interrogation times and narrow velocity distributions [30], [31]. Chip-scale atomic clocks (CSACs), developed recently [27], [29], [32], reduce the size to a few cm$^3$ and power to $\sim$0.1 W, while delivering $10^{-11}$-level Allan deviation and *ppb*/sub-*ppb* level drift over $\sim$100 K range (see Fig. 1). Their internal electrooptical spectrometers consisting of high-stability lasers, integrated temperature-controlled ovens, magnetic shields, etc. [see Fig. 2(a)], stay highly complicated, which makes them still unsuitable for cost-sensitive equipment.

Using a high-precision CMOS spectrometer and carbonyl sulfide ($^{16}$O$^{12}$C$^{32}$S) gas reference, we have demonstrated a fully electronic miniature molecular clock that has similarly high stability but potentially very low cost [14], [33]. In this paper, we first briefly review the recent progress in silicon-based THz spectrometers (see Section II) and then go over some details regarding the principles, designs, and prior experimental results of our molecular clock prototypes (see Sections III and V). In Sections III-C and IV, we present our recent analyses and experimental results on the molecular clock drifts due to the change of temperature and external magnetic field. Both metrics are critical for long-term stability of the clock, but were not investigated previously. We show that, without any ovenized temperature stabilization and back-end compensation, the measured temperature coefficient is $9.5 \times 10^{-11}$/°C. Our testing also reveals $<4 \times 10^{-11}$ clock shift with 75 G of external magnetic field. The above-mentioned findings indicate that the molecular clock

has the potential to deliver stability performance comparable or better than that of CSACs, while using significantly simplified structure or even monolithic implementation in a CMOS chip (see Fig. 2(b) and Section V-A). The high accessibility of the presented time-keeping technology is opening up new opportunities for a wide range of commercial and scientific applications.

## II. Overview of CMOS-Based THz Spectroscopy Systems: From Gas Sensor to Molecular Clock

Research on silicon-based THz integrated circuits was not started until a bit more than a decade ago, but has already achieved significant progress [34]–[36]. The total radiated power from a chip has reached a few mW in the low-THz range [37] and 0.1 mW in the mid-THz range [38]. On-chip THz wave detection, mainly driven by imaging applications, is also realized in both square-law detector arrays [39]–[42] and heterodyne receiver arrays [43], [44]. Other critical THz signal-processing functions, such as phase locking [37], [45], [46], are also demonstrated in chip-integrated building blocks. These advances have paved the way for performing THz rotational spectroscopy using low-cost silicon chips. In this section, we revisit our recent effort in gas-sensing spectrometers and then discuss how that is applied to frequency metrology.

### A. Ultra Broadband, Continuous Wave CMOS Spectrometer

Broadband radiation sources are used in many spectrometers. Examples include filament lamps in infrared spectrometers and picosecond pulse generators in time-domain THz spectrometers. Such a scheme, however, leads to very low concentration of radiated power at the discrete frequencies of interests, hence, low *SNR* and sensitivity. It also has a very limited spectral resolution, which is often determined by the maximum tolerable size of the spectral-analyzing receivers (e.g., lengths of diffraction gratings and interferometers). This is particularly not favorable for rotational spectroscopy because it fails to provide the absolute specificity mentioned in Section I. In comparison, since CMOS chips can generate single-tone signals that are phase-locked (hence, Hz-level spectral width) and tunable, the above-mentioned two problems are eliminated. Previous CMOS rotational spectrometer prototypes were all based on that principle, and covered bands at 200–300 GHz [7]–[9] and at around 500 GHz [10]. The single-tone, wide-tuning-range scheme, however, involves a long scanning time due to the fine resolution (kHz level) required for the absolute specificity, along with the large total band coverage (tens of GHz to 100 GHz) required for molecular detection range. In addition, since optimal efficiency of THz circuits relies on high-$Q$ resonance of passive structures and tunable components like MOS varactor exhibit large loss at THz, the widely tunable circuits required by the above CW spectrometers suffer from significant performance degradation, especially at the two edges of the covered band.

To address the above-mentioned issues, a bidirectional, dual-frequency-comb spectroscopy scheme is adopted [11]–[13], which includes two identical 65 nm CMOS chips (see Fig. 3). Each chip consists of ten cascaded transceivers operating at subbands located from 220 to 320 GHz, respectively (see Fig. 4).

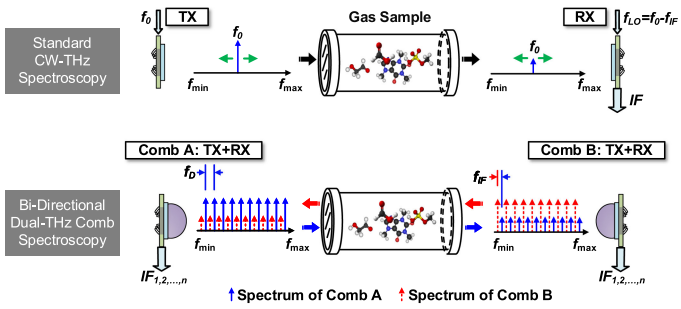


Fig. 3. Comparison of standard CW spectroscopy and the bidirectional dual-comb spectroscopy.

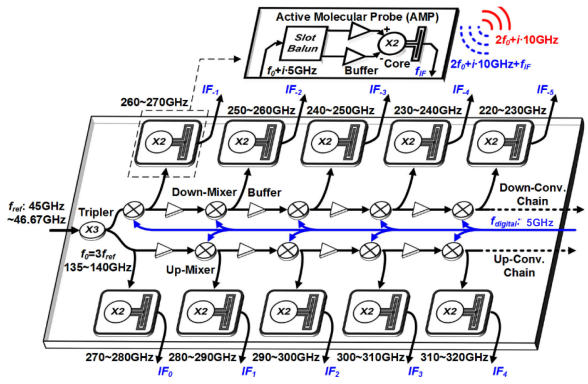


(a)

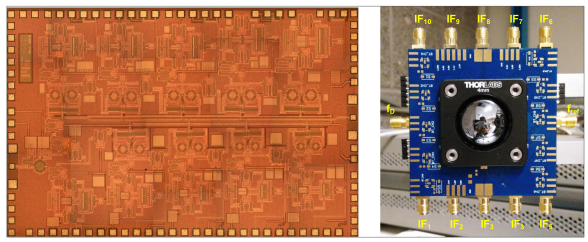

(b)

Fig. 4. (a) Chip architecture of the CMOS THz-comb spectrometer. (b) Photos of the die and the spectrometer package with a hemispheric silicon lens [11], [12].

The chips are placed on the two sides of a gas sample; each chip radiates ten equally spaced tones, and receives and downconverts another ten tones from another chip (see Fig. 3). While the total bandwidth is as large as 100 GHz, every circuit block in Fig. 4(a) only needs to cover 10 GHz bandwidth, which enables the highest possible efficiency across the whole band without the aforementioned tradeoffs. For instance, in the THz front-end block, where an input signal is frequency doubled and then radiated, a double-transmission-line feedback is used to increase the maximum power gain ($G_{ma}$) of the transistor by $\sim$5 dB, which in turn enables a high efficiency in frequency doubling (43% at 275 GHz) [12]. Such a high-parallelism architecture, thanks to the large THz-circuit integration capability of CMOS technology, provides a spectral-sensing approach that has high energy efficiency, fast scanning speed, and high scalability for bandwidth extension. With 100 GHz bandwidth, the

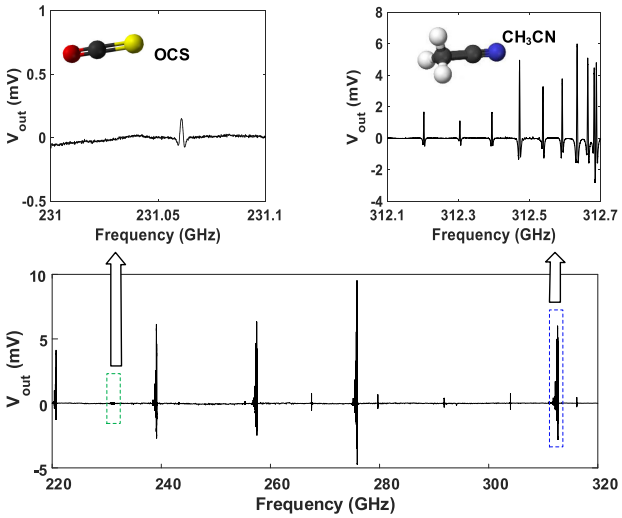


Fig. 5. Measured 220–320 GHz absorption spectrum of a OCS and $CH_3$ CN gas mixture (volume ratio $V_{OCS}/V_{CH_3CN} = 1/60$) [13]. Wavelength modulation with the detection of second-order dispersion curves is used here (see more details in Section III).

spectrometer is capable of detecting any polar molecules with mass similar to or larger than that of hydrogen cyanide (HCN).

The measured total radiated power and noise figure of the chip are 5.2 mW and 14.5–19.5 dB, respectively. In our gas-sensing testing, the dynamic range of the full chipset system is 98 dB. For the detection of molecules with large dipoles, such as acetonitrile ($CH_3$ CN) and HCN, the characterized sensitivity $S_i$ of the system (i.e., minimum detectable concentration) reaches a few *ppm* for 1 s integration time $\tau_{\text{int}}$ ($S_i \propto \tau_{\text{int}}^{-1/2}$) [13]. A standard gas preconcentration with a concentration gain of $10^3$–$10^5$ is expected to further bring this value to one ppb or below. The absolute specificity of the CMOS spectrometer also facilitates high-precision molecular identification and analysis of gas mixtures. This can be illustrated by the results of a demonstration in Fig. 5, which shows the chip-detected absorption spectrum of carbonyl sulfide (OCS) and $CH_3$ CN mixture (with a volume ratio of 1:60). All MHz-wide transition lines unique to each molecule are revealed. The results also well match the reference molecular spectroscopy databases by JPL NASA [47] and Harvard-Smithsonian Center for Astrophysics [48].

### *B. Fully Electronic Time Keeping Using Rotational Transition Lines of Molecules*

One of the most significant impacts of the THz continuous-wave spectrometer is that it provides a fully electronic approach to precisely probe the quantum transition frequency of microscopic particles (polar molecules in this case) and link such an invariant physical constant with a radio-frequency clock (via phase-locked loop (PLL) and frequency multipliers). This opens up the opportunity for the realization of a molecular clock when a negative feedback control loop is built. Fig. 6 shows that basic concept of which the timebase is a certain rotational transition of OCS encapsulated inside a single-mode THz waveguide. A THz spectrometer transmitter is locked to a MHz-level clock

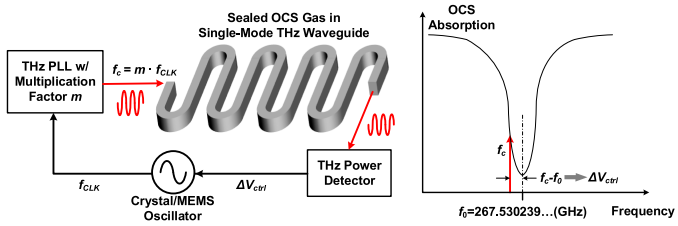


Fig. 6. Simplified block diagram of a THz molecular clock.

(generated by a voltage-controlled crystal/MEMS oscillator), and the clock frequency is dynamically adjusted by the spectrometer receiver, according to the instantaneous frequency offset between the probing frequency $f_c$ and the transition center frequency $f_0$. Then, in the steady state (when $f_c = f_0$), the clock output is locked to $f_0$ through a known frequency multiplication factor $m$ of the THz transmitter chain.

In CSACs, similar principle is applied at much lower excitation frequencies ($f_{\text{cesium}} = 9.192631770$ GHz and $f_{\text{rubidium}} = 6.834682611$ GHz). However, to probe the transition of the atomic spins, assistance of complicated and costly photonics (e.g., high-stability VCSEL laser and photodiode) are required. Buffer gas is also added to the gas cell in order to immobilize the evaporated alkali atoms (hence, smaller Doppler broadening) and to increase the $Q$ of the line, which, however, deteriorates the aging of the device. The recent efforts of atomic clocks have been focused on probing atomic transitions at frequencies well beyond the microwave, which is expected to improve the stability [49]. The invention of the femtosecond optical frequency comb [50] enables optical atomic clocks that directly lock to atomic (e.g., strontium and ytterbium) transitions in light frequencies. Although state-of-the-art prototypes have achieved excellent stability, they require even more sophisticated hardware construction, hence, unsuitable for ultraportable and cost-sensitive applications.

In comparison, the THz molecular clock described above, while probing transition frequencies >20x higher than those in Cs/Rb clocks, offers the simplest implementation and holds promise for highly accessible, atomic-clock-grade devices. It is especially attractive given that all electronics (THz spectrometer, baseband analog/digital circuitry) can now be integrated in a single standard CMOS chip.

## III. THz OCS Clock: Principles and Testing of a Prototype

The first proof-of-concept for the THz molecular clock using OCS as reference was reported last year [14]. This section presents the physics principles and stability characterizations of the clock.

### *A. Selection of Reference Molecule: Why OCS?*

OCS is among the molecules, which are studied most extensively in the field of rotational spectroscopy. OCS is a linear polar molecule and has quantized rotational energy levels $E_J$ following a quadratic pattern with the increasing angular momentum

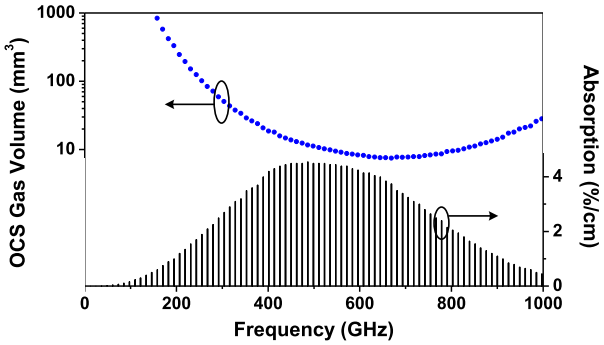


Fig. 7. Absorption intensity of OCS (calculated based on data in [48]) at different frequencies and the associated volume of gas in a single-mode waveguide to achieve ~30% contrast. Note that the absorption here (under a reduced pressure) is about half of the peak absorption value (under a higher pressure), in order to keep the line quality factor to be $\sim 3 \times 10^5$.

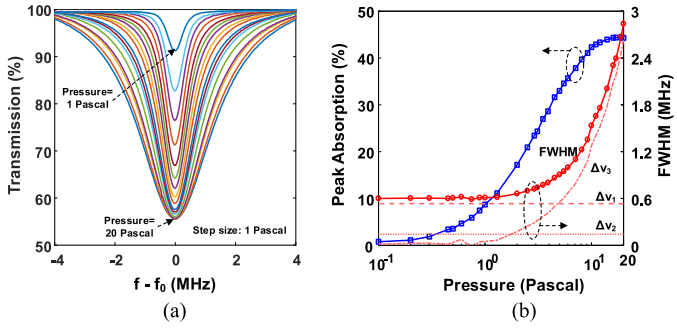


Fig. 8. Measured absorption line profile of OCS around $f_0 = 267.530239$ GHz. (a) Change of intensity and line width at pressure varying from 1 to 20 Pa. (b) Contribution of various broadening mechanisms to the overall line width, including Doppler broadening $\Delta v_1$, wall-collision broadening $\Delta v_2$, and pressure broadening $\Delta v_3$ [14].

number, $J(J = 1, 2, \ldots)$ [1]:

$$E_J = \frac{h^2}{8\pi^2 I_{\text{OCS}}} J(J+1) \tag{1}$$

where $h$ is Planck's constant and $I_{\text{OCS}}$ is the moment of inertia of OCS about axes perpendicular to the internuclear axis. As a result, the frequency $f_0$ of the transition between two adjacent $E_J$ levels is

$$f_{0,J+1\leftarrow J} = \frac{E_{J+1} - E_J}{h} = \frac{h}{4\pi^2 I_{\text{OCS}}}(J+1) \tag{2}$$

which indicates that all transition frequencies are equidistant[2] with a spacing of $h/4\pi^2 I_{\text{OCS}} \approx 12.16$ GHz. Note that each $J$ state also has $2J + 1$ degenerate sublevels, and each sublevel has a magnetic quantum number $m_J$ ($m_J = -J, -J+1, \ldots, -1, 0, 1, \ldots, J-1, J$) and contributes to energy absorption. The total absorption intensity, therefore, increases with $J$ (i.e., transition frequency), as shown in Fig. 7. Beyond ~500 GHz, the intensity drops due to the reduced probability of molecules being at those high-energy states, which is governed by the Boltzmann distribution.

We select OCS as the reference gas of molecular clock for a few reasons.

1) Small Gas Cell Size: OCS has large electrical dipole moment ($\alpha_{\text{OCS}} \approx 0.7$ debye), hence, strong interaction with the radiation. At low-THz range (0.2–0.5 THz), where CMOS chips can operate with acceptable energy efficiency, OCS also has high $J$ values (>16) and many degenerate sublevels. Due to the above-mentioned two reasons, the peak absorption (near 0.5 THz) reaches ~1%/mm, leading to a short path length for a certain signal contrast ratio. This, along with the small cross-sectional area $A_w$ of single-mode waveguides in THz ($A_w \propto f^{-2}$), enables miniaturization of the clock gas cell. In Fig. 7, the volume of a single-mode waveguide gas cell is estimated at different transition frequencies, assuming that the waveguide length is chosen to provide 30% absorption contrast. We see that the required OCS volume is below 100 mm$^3$ at 250 GHz and below 10 mm$^3$ at 400 GHz. It indicates that with advanced packaging, future THz OCS clocks would be only slightly larger than crystal oscillators.
2) Narrow Transition Line: The short-term stability of molecular clock is determined by the $Q$-SNR product of the measured transition curve [33]. The rotational transition line of molecule is broadened by the following conditions.
   a) The Doppler effect due to the molecular Brownian motion (i.e., Doppler broadening).
   b) The intermolecular collision (i.e., pressure broadening).
   c) The collision with the gas cell (i.e., wall broadening).

   Our experimental studies (see Fig. 8) show that the optimal $Q$-SNR product requires a certain low pressure (3–10 Pa in Fig. 8), at which the intermolecular broadening is decreased to a level that is similar to the Doppler broadening [14]. Due to its relatively large mass ($m_{\text{OCS}} = 60$ g/mol), OCS molecule has smaller Brownian motion and, hence, narrower transition lines. Our measured OCS linewidth leads to a quality factor of $\sim 4.7 \times 10^5$. Note that, unlike in CSACs, the $Q$ here is achieved without using any buffer gas. Our testing also shows the feasibility of using small single-mode waveguide as gas cell because the wall broadening only lowers the $Q$ by ~7% [14].
3) High Line Symmetry: By principle, Doppler/pressure-broadened lines should be highly symmetric. However, potential interactions between a rotational mode with other vibrational/rotational/electron-spin modes may lead to multiple transition lines closely adjacent to each other (e.g., $CH_3$ CN in Fig. 5). With the "tail" of one line significantly extending into another line, the overall shape of the latter line becomes asymmetric. Under varying pressure and temperature, the intensity and linewidth of each individual line change, causing a different degree of asymmetry. This leads to a shift of the average center frequency of the line and, hence, a drift of the clock. On this regard,

[2]The centrifugal distortion from molecular rotation stretches the molecular bond (hence, larger moment of inertia) so the frequency spacing in fact decreases slightly with higher $J$. The "equidistant" here is only an approximation assuming the OCS molecule is a rigid motor.

OCS is highly desired because its linear structure possesses simple absorption spectrum, where only one transition line exists for each $J$. Those lines are also far from each other ($\Delta f_0 \approx 12.16$ GHz), resulting in highly symmetric line profile and reduced clock drift. As we will show next, the line asymmetry is also caused by the standing wave formed inside the gas cell, although it can be effectively alleviated through improved gas cell design and advanced circuit-level probing approach (e.g., high-order harmonic dispersion curve detection).

4) Robustness Against Magnetic Field: The electron spin probed in atomic clocks is highly sensitive to magnetic field due to its large magnetic dipole. In the rotation of OCS, only a small offset exists[3] between its mass center (i.e., the rotation center) and the equivalent center of its electric dipole. So the two counter-circulating currents associated with the motions of the positive and negative charges in the dipole almost cancel, leading to a very weak magnetic dipole. This makes OCS rotational modes much less sensitive to magnetic field. This is a distinct advantage over atomic clocks, and will be discussed in more details in Section IV.
5) Simplified Clock Package: Similar to those of CSACs, the gas cell of molecular clock needs to hold low-pressure gas within a small volume for an extended period of time. To address the related challenges, dedicated packaging technologies are needed, which are beyond the scope of this paper. Nevertheless, the usage of OCS is expected to offer several potential advantages. For instance, it maintains its gas phase above $-50$ °C, so no heating process is required for gas evaporation as is the case in alkali atomic clocks. Meanwhile, compared to alkali metals and many other gases, OCS also has very stable chemical properties; this helps reducing the aging of the clock packages.

Lastly, we point out that, apart from OCS, any other gas which meets the above-mentioned criteria may also be utilized as the reference of THz molecular clocks.

### B. Lab-Scale Molecular Clock Prototype

Shown in Fig. 9, a benchtop-size molecular clock probing the OCS transition near 267.530 GHz (for OCS line with $J = 21 \Rightarrow 22$) is constructed using a pair of network analyzer frequency extenders from Virginia diode, Inc. (VDI). The gas cell is a computer numerical control-machined WR-4 meandering waveguide (cross-sectional area: $1.092 \times 0.546$ mm$^2$) with a total path length of 14 cm [see Fig. 9(b)]. The measured waveguide loss (without gas) is 3 dB. Two short sections of optically transparent epoxy are filled in the ends of the waveguide to seal the gas [see Fig. 9(b)], this further increases the gas cell loss to 7.3 dB. When filled with OCS, the measured absorption contrast is 33%. The VDI frequency extenders, driven by RF signal sources, are referenced to an 80 MHz voltage-controlled crystal oscillator (VCXO) cascaded with a divide-by-8 frequency divider. A wavelength modulation scheme (WMS) is used (see

[3]The offset is nonzero since sulfur atom is heavier than oxygen atom.

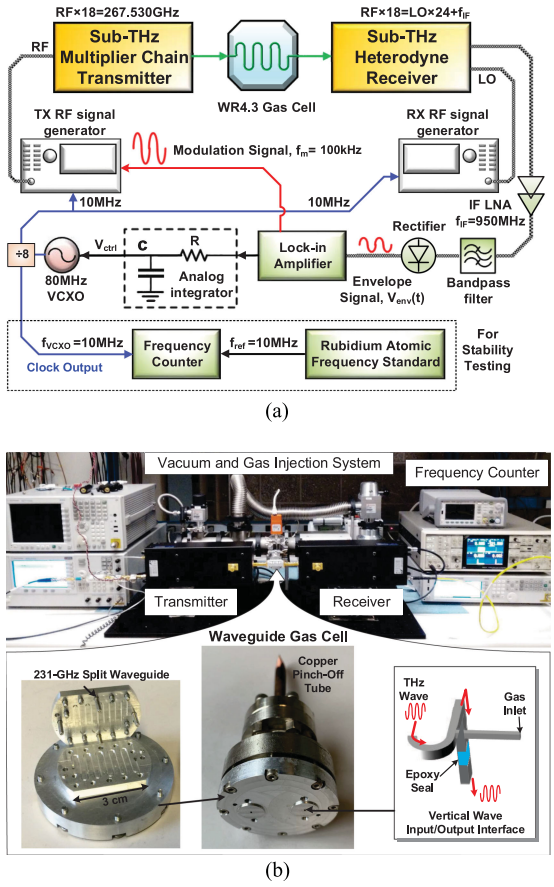


Fig. 9. (a) Block diagram of a lab scale prototype of OCS molecular clock based on a pair of VDI network analyzer frequency extenders. (b) Photos of the prototype including a single-mode waveguide gas cell [14], [33].

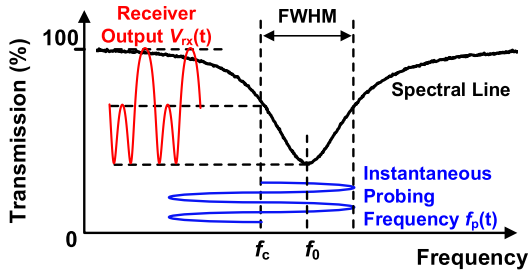


Fig. 10. WMS used for detecting the center frequency of transition line in the molecular clock prototype [14].

Fig. 10) in order to dynamically align the probing frequency $f_c$ with the center $f_0$ of the transition line. Here, the instantaneous probing frequency $f_p(t)$ is modulated around $f_c$ with a modulation frequency $f_m$ of 100 kHz and a modulation depth $\Delta f$ of $\sim$1 MHz. Due to the steep slopes of the absorption line, the envelope of the baseband output signal from the receiver (i.e., WMS dispersion curve) carries harmonic components at $f_m$, $2f_m$, etc. Such a process can also be comprehended as taking the multi-order derivatives of the OCS transition line. Since the odd harmonic components are zero when $f_c$ equals $f_0$ (see Fig. 11), one of such components (with its amplitude and phase extracted by

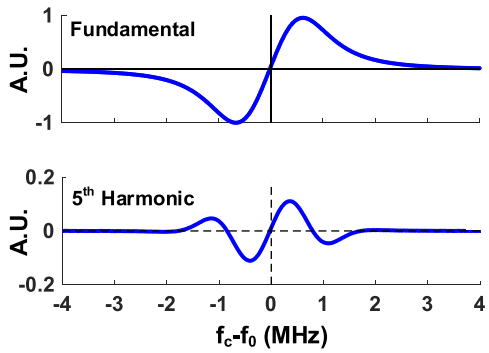


Fig. 11. Measured fundamental and fifth-order harmonic dispersion curves of the OCS transition under probing with wavelength modulation [14].

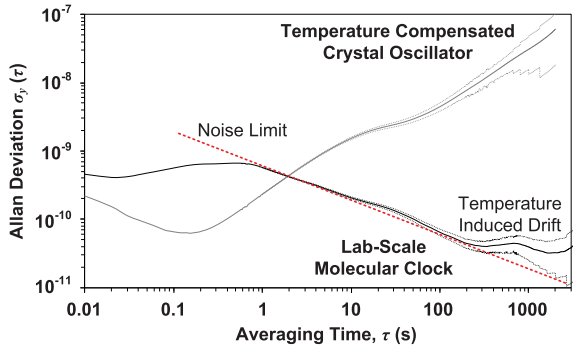


Fig. 12. Measured Allan deviation (solid line) and its confidence interval (dotted black lines) of the lab scale molecular clock without ovenized temperature stabilization and temperature compensation. The expression of the noise limit can be found in [14].

a lock-in amplifier) is used as the indicator of instantaneous frequency error in the feedback control loop to dynamically adjust the tuning voltage of the VCXO.

In the Allan deviation testing, this lab scale clock prototype, when using the fifth harmonic of the WMS dispersion curve, achieves $5.6 \times 10^{-10}$ at an averaging time $\tau$ of 1 s, and $3 \times 10^{-11}$ at $\tau = 1000$ s. The results are shown in Fig. 12. The stability curve flattens out at $\tau$ of $\sim$1000 s because as we show in the next section, the clock has a finite temperature coefficient of $3.7 \times 10^{-11}$/° C at room temperature, and the testing is performed in an uncontrolled open lab environment where the ambient temperature fluctuates. With a back-end temperature compensation, we expect that the Allan deviation can reach into the $10^{-12}$ range. Nevertheless, we see that the dynamic regulation from the molecular clock improves the long-term stability of the VCXO used in the clock by more than three orders of magnitude. Since the closed-loop bandwidth of the molecular clock is $\sim$1 Hz, for $\tau >$1 s, the short-term Allan deviation is determined by the $Q$-SNR product of the detected spectral line (i.e., noise limited) due to the clock dynamic regulation. For $\tau = 0.01$ s and below, the stability curve approaches that of the free-running VCXO due to the filtering of the high-frequency disturbance to the VCXO control voltage. The phase noise of the clock at >100 Hz offset is, therefore, similar to that of the VCXO.

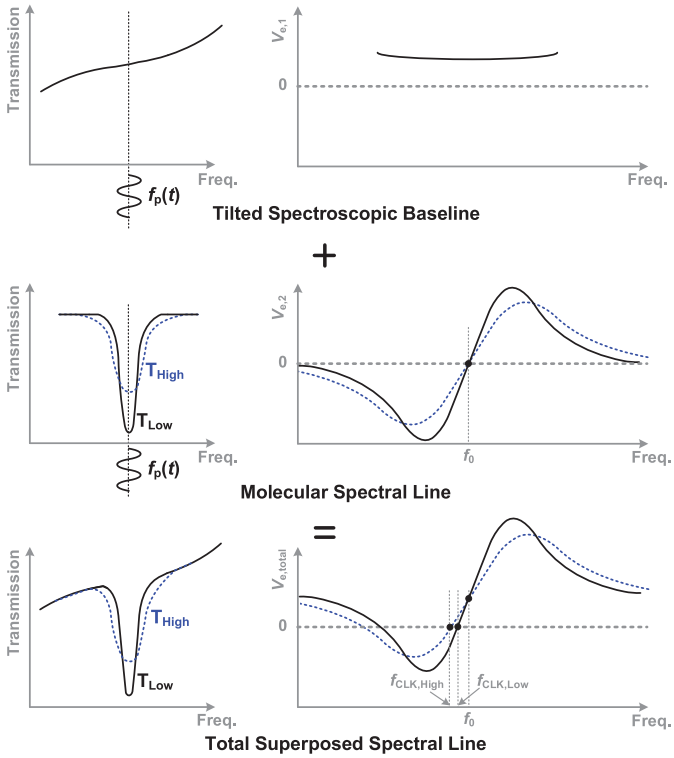


Fig. 13. Effect of spectroscopic baseline tilting on the clock temperature coefficient. Note that the figures are not drawn in scale; both the baseline tilting and frequency offsets are larger than the actual values.

### C. Temperature Coefficient: Analysis and Experiments

The clock output frequency exhibits a weak dependency on temperature for two causes. First, in the sealed gas cell, the pressure $P$ changes linearly with the absolute temperature $T$ (i.e., Gay–Lussac's law). Prior studies [51] showed that OCS transition frequencies $f_0$ shift with $P$, although only a rough estimation for the upper limit of the pressure dependency was given ($|df_0/dP| <$ 15 kHz/Torr or 11 Hz/Pa reported in [52] and [53]). Based on that, as well as the nominal operation pressure and temperature of 10 Pa and 300 K, the upper limit of temperature coefficient due to pressure change should be

$$\frac{df_0}{dT} = \frac{df_0}{dP} \cdot \frac{dP}{dT} = 11 \text{ Hz/Pa} \cdot \frac{10 \text{ Pa}}{300 \text{ K}} = 0.37 \text{ Hz/K}. \quad (3)$$

For a low-THz transition line, (3) is then associated with a relative shift in the realm of $10^{-12}$/°C.

In comparison, the second cause of clock shift, which is related to the symmetry of the transition line, has a more significant impact. Although the intrinsic transition line profile of OCS is highly symmetric, the tilting of the spectroscopic baseline, which is superposed on the intrinsic line profile during the actual molecular probing, introduces certain degree of asymmetry (see Fig. 13). Here, the baseline tilting is caused by the reflection of the THz wave at the waveguide vacuum sealing window (i.e., THz-transparent epoxy in our case); the resultant standing wave then leads to a frequency-dependent transmission pattern. Although the reflection is weak and the spectral

period of the pattern (at GHz according to the gas-cell length) is much larger than the MHz-linewidth of OCS, its effect is still significant given high-precision nature of the clock.

Such an effect is illustrated in Fig. 13. When the wavelength modulation detection scheme is applied, the measured dispersion curve used to create the error signal $V_e$ for VCXO frequency adjustment is also the superposition of the WMS result $V_{e,1}$ of the tilted baseline only (with no OCS) and the WMS result $V_{e,2}$ of the intrinsic OCS transition. With a first-order approximation, the variation of the baseline can be modeled as a straight line, so that $V_{e,1}$ presents as a dc offset added to $V_{e,2}$. Note that in the clock control loop, the total error signal $V_{e,\text{total}} = V_{e,1} + V_{e,2}$ reaches zero in the steady state. But due to the above dc offset, instead of locking to the actual transition frequency $f_0$ where $V_{e,2} = 0$, the clock locks to a slightly different frequency ($f_{\text{CLK,High}}$ in Fig. 13) where $V_{e,2} = -V_{e,1}$.

When the temperature rises, the OCS line has decreased peak absorption intensity and increased linewidth (due to pressure broadening), leading to a smaller slope of the WMS dispersion curve shown as blue dotted curves in Fig. 13. In keeping the zero $V_{e,\text{total}}$, the clock locks to a new frequency ($f_{\text{CLK,High}}$ in Fig. 13) with a larger offset from $f_0$ at a higher temperature $T_{\text{High}}$. This analysis indicates that the reduction of clock temperature coefficient requires smaller baseline tilting, which can be achieved via better impedance matching at the gas cell waveguide sealing [54]. Another effective approach, verified in our experiments, is the detection of high-odd-order harmonic component of the WMS dispersion curve (e.g., the fifth-order signal shown in Fig. 11). As mentioned earlier, such a process is similar to take high-order derivative of the original OCS transition line profile. Since the baseline change is much more gradual than the OCS transition curvature, as we increase the order of WMS detection, $V_{e,1}$ in Fig. 13 approaches zero much more rapidly than $V_{e,2}$ does, leading to higher symmetry. Reduction of temperature coefficient is, hence, realized.

To experimentally study the sensitivity of the molecular clock to temperature, in the same setup shown in Fig. 9(a), the gas cell is wrapped by an additional silicone heating tape (HSTAT Series); meanwhile, a K-type thermocouple (from Harrick Scientific Products) is also mounted to the gas cell to monitor the real-time temperature of OCS gas. Fifth-order harmonic WMS detection is used in the clock. Fig. 14 shows the measured gas cell temperature and the corresponding output frequency deviation (from the mean near 10 MHz) when the heater is turned ON. Over a temperature range from 28–70 °C, the clock output frequency varies by approximately 0.04 Hz (i.e., 4 ppb), resulting in an average temperature coefficient of 0.095 ppb/°C. It is noteworthy that the temperature coefficient is only ∼0.037 ppb/°C at 28–55 °C, and increases to 0.20 ppb/°C at 55–70 °C.

Currently, efforts are being made to develop miniature gas cells with improved sealing, impedance matching, and reduced out-gassing. With these efforts, the temperature coefficient of the OCS clock is expected to be further reduced. This, along with a back-end temperature compensation, which normally lowers the temperature coefficient by 10∼100x, is expected to suppress the drift across 100 K temperature change to the level of $10^{-10}$.

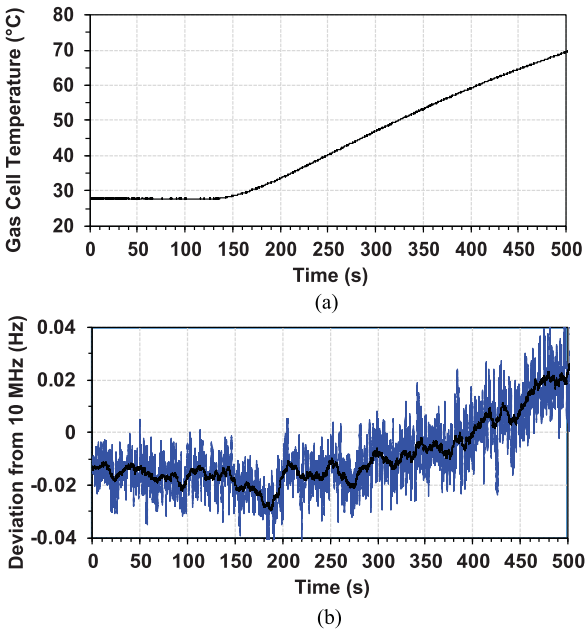


Fig. 14. (a) Measured instantaneous temperature and pressure of the gas cell as it is heated up. (b) Deviation of the clock output frequency from its mean value near 10 MHz. The blue curve is based on data sampled every 1 s, and the black curve is the average value using a 10 s integration window.

## IV. Clock Sensitivity to Magnetic Field

Clock robustness against strong magnetic fields is critical to many applications under extreme operation conditions. For instance, high-stability frequency references are becoming critical for future wireless networks among electric autonomous vehicles, and the magnetic field strength in their operation environments could be above 30 G [55] due to the presence of electric motors and large currents. In this section, we first discuss the magnetic-induced shift (i.e., intrinsic shift) of the molecular clock based on the superposition of all sublevels in a certain OCS transition. Both the first-order and second-order Zeeman shifts of those sublevels are considered. Then, an experiment based on our lab scale molecular clock prototype is presented.

### *A. Intrinsic Magnetic-Induced Clock Shift: A Theoretical Study*

With the presence of a magnetic field $H$, the rotational energy levels associated with different magnetic quantum numbers $m_J$ deviate from their degenerate value at zero field. For rotational state of $J$, the energy deviation $E(J, m_J)$ is expressed as [56]

$$E(J,m_J) = -\mu_0 g_{\text{OCS}} m_J H - \frac{[3m_J^2 - J(J+1)](\chi_\perp - \chi_\parallel)}{3\cdot(2J-1)(2J+3)} H^2 \tag{4}$$

where the first term is the first-order Zeeman shift, $\mu_0$ is the nuclear magneton ($5.051 \times 10^{-27}$ J· T$^{-1}$), and the $g$-factor for OCS is previously determined to be $g_{\text{OCS}} \approx -0.029$ [57]–[59]. Compared to electronic spins ($g \approx 2$) used in atomic clocks, rotation of OCS molecules possesses much smaller magnetic dipole

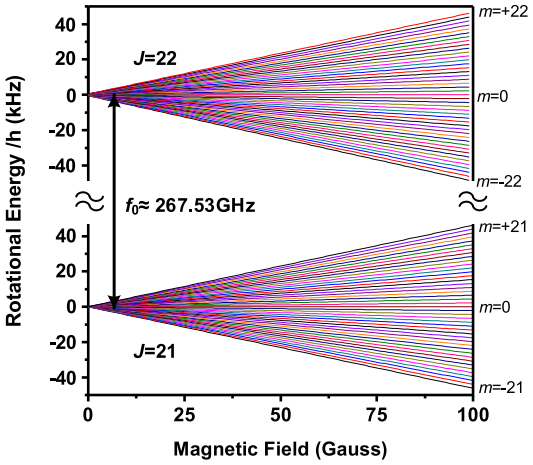


Fig. 15. Calculated rotational energy change (in terms of photon frequency) at $J = 21$ and $J = 22$ with an external magnetic field. First-order Zeeman shifts in (4) is dominant for $m \neq 0$.

moment and $g$-factor, as is explained in Section III-A. The second term in (4) stems from an additional, field-induced magnetic moment of OCS [60], where $\chi_\perp$ and $\chi_\parallel$ are the magnetic susceptibilities perpendicular and parallel to the internuclear axis. In [56], the measured value of $\chi_\perp - \chi_\parallel$ is about $1.54 \times 10^{-29}$ erg/G$^2$.

For $J = 21 \Rightarrow 22$ transition ($f_0 \approx 267.53$ GHz), the above energy split is illustrated in Fig. 15. Due to the selection rule, permitted changes of $m_J$ are $\Delta m_J = 0$ ($\pi$ component) and $\Delta m_J = \pm 1$ ($\sigma$ component). Note that a static magnetic field in parallel with the electric field of THz radiation ($H_{\text{static}} \parallel E_{\text{THz}}$) gives rise to $\Delta m_J = 0$ transitions, and a magnetic field perpendicular to the THz electric field ($H_{\text{static}} \perp E_{\text{THz}}$) gives rise to $\Delta m_J = \pm 1$ transitions [1]. In Fig. 16, the frequency deviation of all possible $J = 21 \Rightarrow 22$ transitions ($3 \times (2J + 1) = 129$ in total) associated with Fig. 15 are plotted. Given the weak split (kHz level for $\Delta m_J = \pm 1$ under $\approx 100$ Gauss) in comparison with the MHz-level linewidth of each sublevel at THz, transition lines of all $m_J$ sublevels overlap and contribute to the overall absorption curve used in the OCS molecular clock. This not only increases the overall intensity as mentioned in Section III, but also, to a large extent, maintains the symmetry and the equivalent center frequency of the absorption curve. This is because, as shown in Fig. 16(a), the first-order deviations of $\Delta m_J = 0$ transitions are zero and those of $\Delta m_J = +1$ and $\Delta m_J = -1$ transitions cancel each other.

The sensitivity of OCS clock to magnetic field is only attributed to the weak, second-order Zeeman shift described as the second term of (4). Shown in Fig. 16(c), (d), and (b), larger magnetic field induces an asymmetry to the overall absorption curve and changes its equivalent center frequency (hence, clock frequency drift). To quantify such a drift, we compute the high-precision profile $\gamma_n(f)$ of the overall absorption curve as the superposition of all excited sublevel transitions. Each transition possesses a Lorentzian shape with linewidth of FWHM $\approx$ 1 MHz, a frequency deviation of:

$$\Delta f_{m_J} = \begin{cases} [E(J+1, m_J) - E(J, m_J)]/h & \text{for } \Delta m_J = 0 \\ [E(J+1, m_J \pm 1) - E(J, m_J)]/h & \text{for } \Delta m_J = \pm 1 \end{cases} \tag{5}$$

and a normalized intensity of [1], [61]

$$\text{Intensity} = \begin{cases} \dfrac{(J+1)^2 - m_J^2}{(J+1)(2J+1)(2J+3)} & \text{for } \Delta m_J = 0 \\ \dfrac{(J+1-m_J)(J+2-m_J)}{2(J+1)(2J+1)(2J+3)} & \text{for } \Delta m_J = \pm 1 \end{cases}. \tag{6}$$

The calculated values of (5) and (6) at 100 G are shown in Fig. 17.

Next, we calculate the overall absorption line profile as the superposition of the above sublevels. When $\Delta m_J = 0$ transitions are excited (i.e., $H_{\text{static}} \parallel E_{\text{THz}}$), the line profile is

$$\gamma_{n,\pi}(f) = \sum_{m_J=-J-1}^{J+1} \left[ \frac{(J+1)^2 - m_J^2}{(J+1)(2J+1)(2J+3)} \cdot \frac{1}{1 + \left( \frac{f - f_0 - \Delta f_{m_J=0}}{\text{FWHM}/2} \right)^2} \right]. \tag{7}$$

When $\Delta m_J = \pm 1$ transitions are excited (i.e., $H_{\text{static}} \perp E_{\text{THz}}$), the line profile is

$$\gamma_{n,\sigma}(f) = \sum_{m_J=-J-1}^{J+1} \left[ \frac{(J+1-m_J)(J+2-m_J)}{2(J+1)(2J+1)(2J+3)} \cdot \frac{1}{1 + \left( \frac{f - f_0 - \Delta f_{m_J=-1}}{\text{FWHM}/2} \right)^2} + \frac{(J+1+m_J)(J+2+m_J)}{2(J+1)(2J+1)(2J+3)} \cdot \frac{1}{1 + \left( \frac{f - f_0 - \Delta f_{m_J=+1}}{\text{FWHM}/2} \right)^2} \right]. \tag{8}$$

To emulate the clock operation, the dispersion curves using wavelength modulation applied to $\gamma_{n,\pi}(f)$ and $\gamma_{n,\sigma}(f)$ are derived in MATLAB. Then, the zero-crossing frequencies of the dispersion curves, which represent the clock output at varying magnetic field strength, are obtained. The values of the shifts are plotted in Fig. 18. Based on the results, we have the following two observations.

First, the OCS molecular clock exhibits excellent robustness against external magnetic field. At 100 G (intensity of an iron magnet), the calculated intrinsic clock deviation is only about 0.1 Hz out of 267.53 GHz, or $4 \times 10^{-13}$ (relative change). Therefore, unlike cesium and rubidium CSACs, the OCS clock does not require a magnetic shield for most applications.

Second, Figs. 17 and 18 indicate that the clock shifts due to the $\Delta m_J = 0$ and $\Delta m_J = \pm 1$ transitions have opposite signs and similar magnitudes. Therefore, the values in Fig. 18 are the shifts in the worst case. For other $H$ orientations having both longitudinal $H_\parallel$ and transverse $H_\perp$ components with respect to $E_{\text{THz}}$ (so that all transitions are excited), the clock deviation is reduced with the partial cancellation of the above two sets of shifts. Note that such a property may be utilized to minimize the impact by orientating the clock gas cell in a way that $H_\parallel \approx H_\perp$.

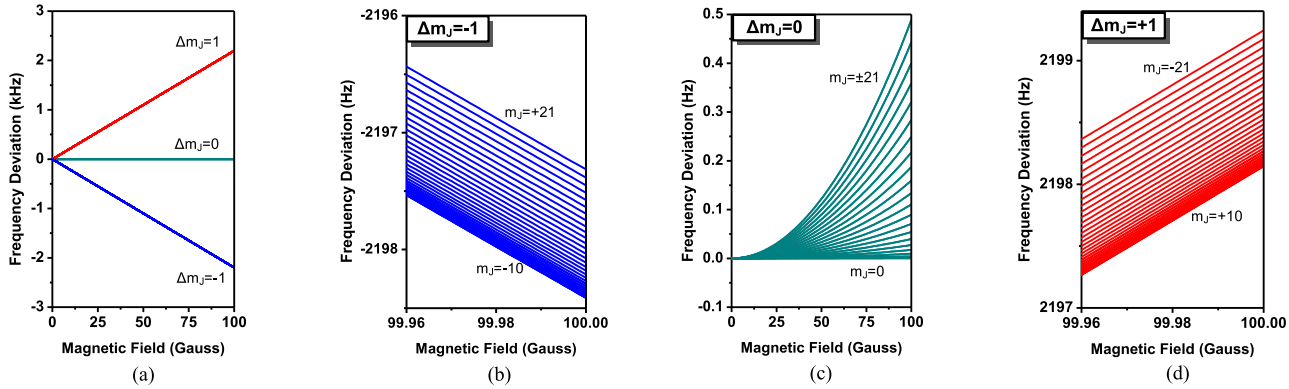


Fig. 16. (a) Frequency deviation of all $J = 21 \Rightarrow 22$ transitions (129 lines in three groups) around $f_0 \approx 267.53$ GHz. (b)–(d) Zoom-in views of (a) for $\Delta m_J = 0$, $\Delta m_J = +1$, and $\Delta m_J = -1$, respectively. For the $m_J$ value associated with each transition, refer to Fig. 17.

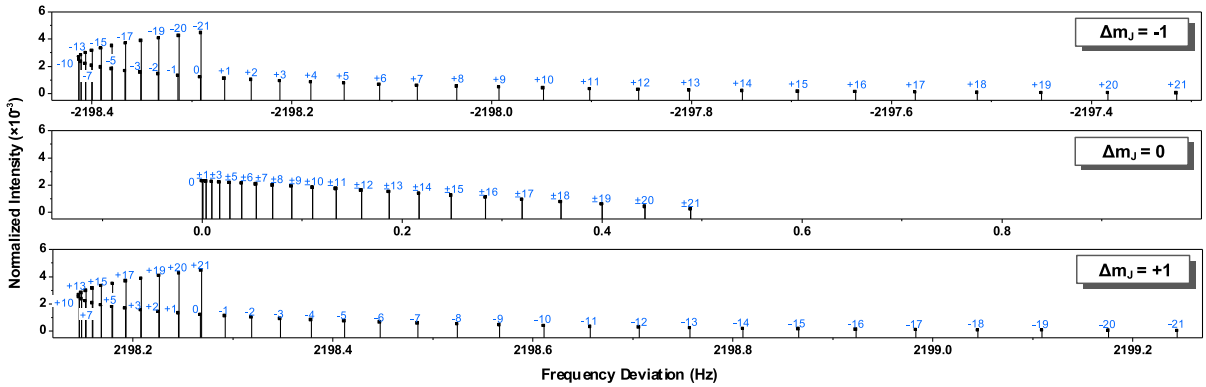


Fig. 17. Frequency deviation (from ∼267.53 GHz) and intensities of Zeeman components for $J = 21 \Rightarrow 22$ and a magnetic field of 100 G. The integer on top of each line is the associated $m_J$ number at $J = 21$. The calculations are based on (5) and (6).

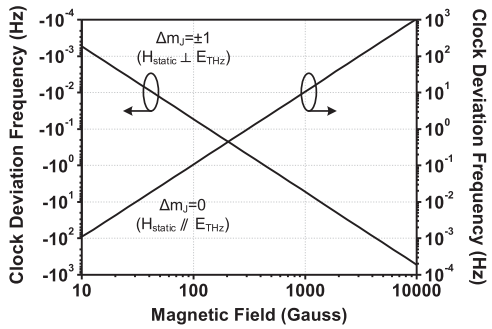


Fig. 18. Absolute frequency deviation of a 267.53 GHz OCS clock at varying magnetic field intensities.

### B. Preliminary Experimental Results

The intrinsic frequency deviation calculated above is too small (even with 100 Gauss external magnetic field) to be measured reliably, given the presence of other nonideal factors, such as temperature change and gas-cell out-gassing or leakage. Nevertheless, an experiment with an external electrically controlled magnetic field applied to the OCS gas cell is still important to at least verify the clock robustness stated above.

Shown in Fig. 19(a), to apply a uniform magnetic field onto the WR-4.3 waveguide gas cell,[4] a pair of Helmholtz coils with a radius of 125 mm and 210 turns are placed symmetrically on the two sides of the gas cell. The distance between the coils is 125 mm. The coils are driven by a 5 A dc current, which is switched ON and OFF every 2 min. Accordingly, the applied field strength is ∼75 G.

Fig. 19(b) presents the measured frequency deviation from the mean frequency, sampled every 1 s. During the entire measurement duration of 12 min, the 10 MHz output frequency of the clock increases by 1.7 mHz (i.e., 0.17 ppb). We suspect that such a drift is mainly due to the increased pressure from out-gassing (see Section III-C). To examine the field-induced frequency shift, averaged frequencies within every 2 minute window are plotted in the black trace in Fig. 19(b). The gray trace in the zoomed figure corresponds to a least square fit to the averaged frequencies when the external field was OFF. The largest frequency deviation from the fitted trace is 0.4 mHz (i.e., 40 ppt).

[4]The gas cell is made out of 7075 aluminum alloy and, therefore, does not shield the magnetic field.

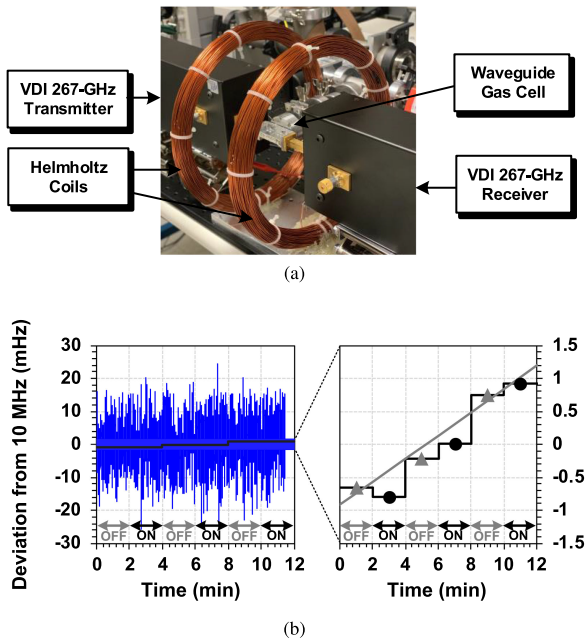


Fig. 19. (a) Magnetic sensitivity testing setup. The gas cell of the molecular clock is placed inside a pair of Helmholtz coils applying 75 G magnetic field. (b) Measured frequency deviation with the external field turned ON and OFF every 2 min.

At this point, no conclusive correlation between the application of magnetic field and frequency shift is observed, especially given that the Allan deviation of 2 min averaging time is several tens of ppt (see Fig. 12). Nevertheless, even the most conservative estimation indicates that the field-induced frequency shift is <40 ppt with 75 G magnetic field. Note that the above upper bound value is still ∼100x higher than the intrinsic field-induced shift calculated in Section IV-A, which calls for more in-depth studies in the future. Up to this point, the experiment presented here at least demonstrates that, even without a built-in magnetic shield, the THz OCS clock still provides significantly higher robustness against magnetic field compared to other miniature atomic clocks with dedicated magnetic shields (e.g., $\pm 9 \times 10^{-11}$/Gauss for <2 Gauss in [27]).

## V. Chip-Scale Molecular Clock

To further demonstrate the feasibility of miniaturization, as well as the low power and low cost of the clock, a fully integrated molecular clock chipset is implemented using a TSMC 65-nm low-power bulk CMOS technology [33], [62]. For optimal energy efficiency of the chipset, the OCS transition at ∼231.060983 GHz ($J = 18 \Rightarrow 19$) is used as the timebase. Fig. 20 shows the architecture of the chipset consisting of a transmitter and a receiver. The core of the transmitter is a 57.8-GHz PLL, which then drives two cascaded frequency doublers to generate a 231 GHz probing signal. The PLL is equipped with a 40-bit $\Delta$-$\Sigma$ modulator, which allows frequency tuning with $10^{-12}$-level precision. By changing the average PLL division ratio during a postfabrication calibration, high frequency accuracy at the clock output is obtained.

The modulator also enables frequency-shift keying modulation of the 231-GHz frequency, so that the clock periodically ($f_m = 16$ kHz) probes at the two edges of the OCS line. The steady state is reached when the detected absorption associated with the above two frequency points is balanced. Note that such an operation is similar to the detection of the fundamental component of the WMS dispersion curve, described in the lab scale clock prototype in Section III. However, high-order harmonic detection, which suppresses pressure/temperature-induced drifts, is not available because the probing signal does not sweep the entire curvature of the OCS line and, hence, generates no harmonic information. To realize that function, future chip designs may adopt an analog FM modulation directly applied to the voltage-controlled oscillator inside the PLL.

Another architectural difference from the lab scale prototype is that the chip-based clock receiver uses a MOSFET square-law detector instead of a heterodyne receiver. Square-law detectors have inferior sensitivity in radio and imaging receivers because the output $V_{\text{out}}$ is generated via the self-mixing of the weak input signal $V_{\text{sig}}$

$$V_{\text{out}} \propto V_{\text{sig}}^2 \tag{9}$$

instead of the mixing with a high-power local oscillator (LO) signal in the case of a heterodyne receiver.

In spectrometers and clocks, the situation is different because the signal to be detected $V_{\text{sig}}$ is the variation of the large THz probing signal $V_{\text{TX}}$ generated by the transmitter. The output signal of the square-law detector is then determined by

$$V_{\text{out}} \propto V_{\text{TX}}^2 - (V_{\text{TX}} - V_{\text{sig}})^2 \Rightarrow 2V_{\text{TX}}V_{\text{sig}} \tag{10}$$

which is similar to that of a heterodyne receiver. In the light of such reduced performance gap, a square-law detector is chosen for its simplicity and lower dc power.

The die photos of the CMOS chips and the clock package are shown in Fig. 21(a) and (b), respectively. A gas cell similar to that in Fig. 9(b) is used. The signal coupling between the WR-4 waveguide and the chip is realized via a quartz waveguide feed, which transforms the quasi-TEM wave mode in a microstrip to a TE mode in the gas cell waveguide [63]. Three bond wires forming a coplanar waveguide-like transmission line connect the chip with the quartz feed. Although the simulated insertion loss of the entire coupler is only ∼1 dB, the measured value increases to ∼10 dB. The discrepancy may be caused by the bond-wire length (∼200 $\mu$m) longer than the designed value (100 $\mu$m), which leads to ∼8 dB loss in our simulation. The higher loss may also be caused by the nonideal connection of the feed and waveguide via conductive epoxy. With such coupling loss, the measured output power and sensitivity (quantified using noise equivalent power NEP) of the chipset at the waveguide interfaces are ∼10 $\mu$W and 0.5 nW/Hz$^{1/2}$, respectively (see Fig. 22). Albeit the underoptimal package performance, the SNR of the OCS line dispersion curve measured by the clock [see Fig. 23(a)] is still 53 dB. The measured Allan deviation of the chip-scale molecular clock is $2.5 \times 10^{-9}$ at $\tau = 1$ s and $3.8 \times 10^{-10}$ at $\tau = 1000$ s. In the future, the coupler loss can be significantly reduced by integrating a waveguide feeding structure on-chip, so that the THz signal is directly radiated into the waveguide

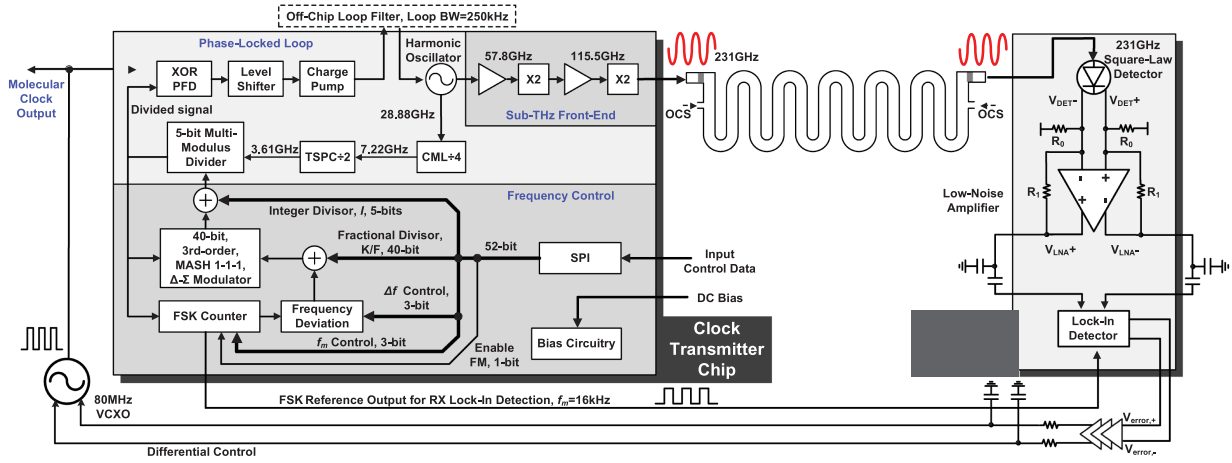


Fig. 20. System architecture of the chip-scale molecular clock using 65 nm CMOS technology [33].

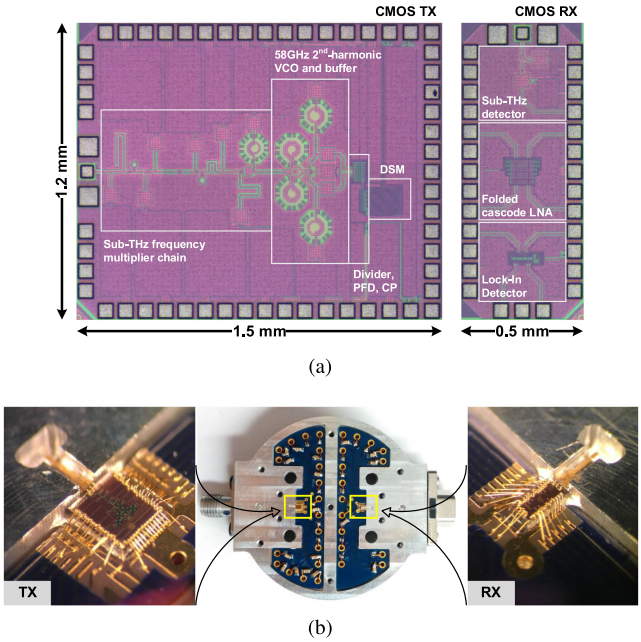


(a)

(b)

Fig. 21. (a) Die photos. (b) Package of the chip-scale molecular clock using 65 nm CMOS technology [33].

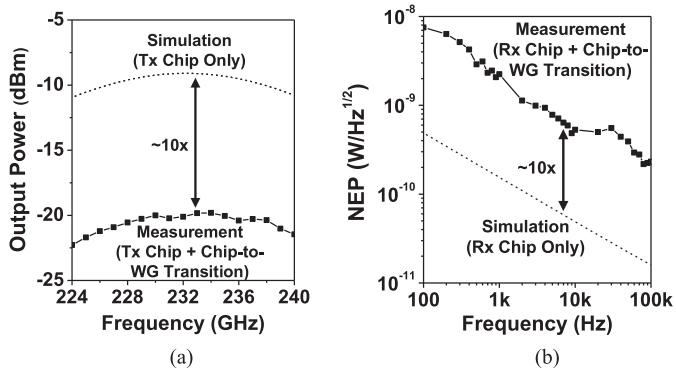


(a) (b)

Fig. 22. Measured and simulated results of (a) the output power and (b) the noise equivalent power of the CMOS molecular clock [33], [62].

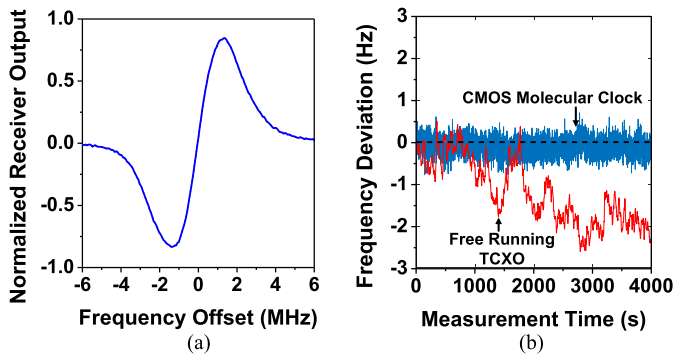


(a) (b)

Fig. 23. (a) Dispersion curve measured by the CMOS clock chipset. The center frequency of the plot is close to 231.060983 GHz. (b) Measured instantaneous clock output frequency deviation from 80 MHz. [33], [62]

opening. The short-term stability ($\tau = 1$ s) is expected to reach $4 \times 10^{-11}$ when the chip-waveguide coupler loss is improved to 1 dB [33]. Fig. 23(b) demonstrates the improved stability over the free-running TCXO used in the clock.

### *A. Enabling Device Technologies for Higher Efficiency, Stability and Further Miniaturization*

The measured total dc power consumption of the clock chipset is 66 W, out of which 25 mW is consumed in the 57.8–231 GHz multiplier and buffer stages. This is only about half of that of CSAC in [27]. At present, only nonlinear harmonic operations can be used for the 231 GHz generation due to the limited speed performance of the 65 nm CMOS transistors ($f_{\max} \approx 220$ GHz).

The above situation, fortunately, is expected to improve soon with the recent development of high-speed silicon transistors. For example, 22-nm FinFETs and 100-nm SiGe HBTs with measured maximum oscillation frequencies $f_{\max}$ of 450 GHz [64] and 720 GHz [65] have been reported, respectively. This starts to allow for fundamental-mode oscillation and power amplification

in the low-THz range (∼300 GHz), which is expected to reduce the dc power consumption to <40 mW. The clock receiver will also be much more sensitive (hence, improved short-term Allan deviation) due to the availability of low-noise amplifiers (LNA).[5]

On the other hand, applying the current harmonic-generation approach to the new high-speed devices enables the realization of molecular clocks at ∼500 GHz without additional power consumption (compared to our current chipset). This allows us to reach the optimal operation point, as shown in Fig. 7, for the minimum clock size.[6] It is noteworthy that the height of the related waveguide (∼0.15 mm) is smaller than standard chip substrate thickness (0.3–0.5 mm), and low-loss micro-machined THz waveguides in silicon has already been demonstrated [66]. Therefore, it is even possible that a THz OCS molecular clock is entirely integrated inside a CMOS system-on-chip [see Fig. 2(b)].

## VI. Conclusion

In this paper, we review the principles, prototypes, and testing results of a THz OCS molecular clock, which builds upon the recent advances of CMOS-based rotational spectrometers and provides an alternative time-keeping approach to CSACs for portable applications. In particular, the advantages of using OCS as the reference gas are explained, which show that a fully electronic clock with $mm^3$ level gas cell size is feasible.

At present, our measured short-term stability is $5.6 \times 10^{-10}$ ($\tau = 1$). In [14], we predict that the above value can be improved to $10^{-11}$, if a THz receiver with lower noise is used.[7] This merit is ultimately limited by the Doppler broadening of the OCS spectral line, leading to a quality factor much lower than those obtained in sophisticated atomic clocks using, for example, laser cooling and atomic fountain. Another distinct trait of our miniature clock, compared with other atomic clocks, is that the reference particles (i.e., OCS molecules) are not isolated from the environment. In this paper, the long-term stability associated with the responses of the OCS spectral line to the temperature and magnetic field is studied. We show that, due to the baseline tilting of the waveguide gas cell, the asymmetry of the measured OCS transition line increases the sensitivity to temperature change. A measured temperature coefficient of $9.5 \times 10^{-11}$/°C is obtained in a preliminary experiment for 28 °C to 70 °C. Next, analyses regarding the magnetic-induced clock shift are presented. While the first-order Zeeman effects of all transition sublevels maintain the symmetry of the transition line and introduce no shift, we show that the clock shift caused by the second-order Zeeman effects is, by theory, $4 \times 10^{-13}$. Our preliminary experiment indicates that the upper limit value of the magetic-induced shift is $4 \times 10^{-11}$; this at least verifies our previous prediction [14] about the clock's high robustness under strong magnetic conditions.

The above-mentioned studies, along with the CMOS-based clock prototype we review in the end of this paper, complement our previous research [14], [33] and further demonstrate that the OCS molecular clock should not require ovenized temperature stabilization and magnetic shield for long-term stability at sub-*ppb* level. With these advances, an ultra-low-cost, fully monolithic "atomic" clock is no longer unimaginable.

[5]Based on our research in [14], the optimal probing power of OCS clock is ∼50 $\mu$W, which does not pose stringent linearity requirement for the LNA.

[6]Although the absolute wall broadening increases with smaller waveguide size, the relative increase to the linewidth is the same as the low-frequency case due to the proportionally increased center frequency.

[7]The high-order subharmonic heterodyne receiver ($f_{LO} = f_{in}/18$) used in our current lab scale prototype has a noise figure over 40 dB. In comparison, on-chip heterodyne receivers with lower order subharmonic LOs ($f_{LO} = f_{in}/2$) and <20 dB noise figure have been reported [12].

## Acknowledgment

The authors would like to thank Dr. J. Lin at the National Science Foundation (NSF). They also appreciate the help from Dr. S. Coy, Prof. R. Field, and Prof. K. Nelson at the Department of Chemistry, MIT, Dr. B. Perkins at MIT Lincoln Lab, Prof. J. Muenter from the Department of Chemistry, University of Rochester, Dr. J. Herbsommer from Texas Instruments, and Dr. L. Yi from JPL NASA. Last but not the least, the authors express their deep gratitude and commemoration to Dr. D. Buss (MIT visiting scientist from Texas Instruments) for his generous support and all the inspiring discussions.

## References

[1] C. H. Townes and A. L. Schawlow, *Microwave Spectroscopy*, 2nd ed. New York, NY, USA: Dover, 2012.

[2] C. Kulesa, "Terahertz spectroscopy for astronomy: From comets to cosmology," *IEEE Trans. THz Sci. Technol.*, vol. 1, no. 1, pp. 232–240, Sep. 2011.

[3] I. R. Medvedev, C. F. Neese, G. M. Plummer, and F. C. De Lucia, "Submillimeter spectroscopy for chemical analysis with absolute specificity," *Opt. Lett.*, vol. 35, no. 10, pp. 1533–1535, 2010.

[4] C. F. Neese *et al.*, "Compact submillimeter/terahertz gas sensor with efficient gas collection, preconcentration, and ppt sensitivity," *IEEE Sensors J.*, vol. 12, no. 8, pp. 2565–2574, Aug. 2012.

[5] B. H.-B. Liu, H. Zhong, N. Karpowicz, Y. Chen, and X.-C. Zhang, "Terahertz spectroscopy and imaging for defense and security applications," *Proc. IEEE*, vol. 95, no. 8, pp. 1514–1527, 2007.

[6] J. Pereira *et al.*, "Breath analysis as a potential and non-invasive frontier in disease diagnosis: An overview," *Metabolites*, vol. 5, no. 1, pp. 3–55, 2015.

[7] N. Sharma *et al.*, "200-280 GHz CMOS RF front-end of transmitter for rotational spectroscopy," in *Proc. Symp. VLSI Technol.*, 2016, pp. 329–331.

[8] Q. Zhong, W. Choi, C. Miller, R. Henderson, and K. K. O, "A 210-to-305 GHz CMOS receiver for rotational spectroscopy," in *Proc. IEEE Int. Solid-State Circuits Conf.*, San Francisco, CA, USA, 2016, pp. 426–427.

[9] K. Schmalz *et al.*, "245-GHz transmitter array in SiGe BiCMOS for gas spectroscopy," *IEEE Trans. THz Sci. Technol.*, vol. 6, no. 2, pp. 318–327, Mar. 2016.

[10] P. Neumaier *et al.* "Tunable 500 GHz sensor system in SiGe technology for gas spectroscopy," *Electron. Lett.*, vol. 51, no. 17, pp. 1345–1347, 2015.

[11] C. Wang and R. Han, "Rapid and energy-efficient molecular sensing using dual mm-wave combs in 65 nm CMOS: A 220-to-320 GHz spectrometer with 5.2 mW radiated Power and 14.6-to-19.5 dB noise figure," in *Proc. Int. Solid-State Circuit Conf.*, San Francisco, CA, USA, 2017, pp. 18–20.

[12] C. Wang and R. Han, "Dual-terahertz-comb spectrometer on CMOS for rapid, wide-range gas detection with absolute specificity," *IEEE J. Solid-State Circuits*, vol. 52, no. 12, pp. 3361–3372, Dec. 2017.

[13] C. Wang, B. Perkins, Z. Wang, and R. Han, "Molecular detection for unconcentrated gas with ppm sensitivity using dual-THz-comb spectrometer in CMOS," *IEEE Trans. Biomed. Circuits Syst.*, vol. 12, no. 3, pp. 709–721, Jun. 2018.

[14] C. Wang *et al.*, "An on-chip fully-electronic molecular clock based on sub-thz rotational spectroscopy," *Nature Electron.*, vol. 1, no. 7, pp. 421–427, 2018.

[15] *Underwater Exploration With Chip Scale Atomic Clocks (CSAC)*, Microsemi Corporation, Aliso Viejo, CA, USA, 2017. [Online]. Available: www.microsemi.com

[16] H. Li, L. Han, R. Duan, and G. M. Garner, "Analysis of the synchronization requirements of 5G and corresponding solutions," *IEEE Commun. Standards Mag.*, vol. 1, no. 1, pp. 52–58, Mar. 2017.

[17] J. C. Salvia, R. Melamud, S. A. Chandorkar, S. F. Lord, and T. W. Kenny, "Real-time temperature compensation of MEMS oscillators using an integrated micro-oven and a phase-locked loop," *J. Microelectromech. Syst.*, vol. 19, no. 1, pp. 192–201, 2010.

[18] M. H. Li, C. Y. Chen, C. S. Li, C. H. Chin, and S. S. Li, "A monolithic CMOS-MEMS oscillator based on an ultra-low-power ovenized micromechanical resonator," *J. Microelectromech. Syst.*, vol. 24, no. 2, pp. 360–372, 2015.

[19] C.-S. Liu, R. Tabrizian, and F. Ayazi, "A 0.3 ppm oven-controlled MEMS oscillator using structural resistance-based temperature sensing," *IEEE Trans. Ultrason., Ferroelect., Freq. Control*, vol. 65, no. 8, pp. 1492–1499, Aug. 2018.

[20] Y. Chen *et al.*, "Ovenized dual-mode clock (ODMC) based on highly doped single crystal silicon resonators," in *Proc. IEEE Int. Conf. Micro Electro Mech. Syst.*, 2016, pp. 91–94.

[21] K. E. Wojciechowski and R. H. Olsson, "A fully integrated oven controlled microelectromechanical oscillator-part II: Characterization and measurement," *J. Microelectromech. Syst.*, vol. 24, no. 6, pp. 1795–1802, 2015.

[22] Z. Wu and M. Rais-Zadeh, "A temperature-stable MEMS oscillator on an ovenized micro-platform using a PLL-based heater control system," in *Proc. IEEE Int. Conf. Micro Electro Mech. Syst.*, 2015, pp. 793–796.

[23] *Emerald OCXOs for Precision Time Synchronization Emerald OCXOs for Precision Time Synchronization*, SiTime Corporation, Santa Clara, CA, USA, 2018.

[24] *ECS-TXO-5032 Datasheet*, ECS International Incorporation, Lenexa, KS, USA.

[25] *KT2520K Datasheet*, Kyocera Crystal Device Corporation, Higashine, Japan, 2015.

[26] *ECOC-2522 SMD OCXO Datasheet*, ECS International Incorporation, Lenexa, KS, USA, 2016.

[27] *Quantum SA.45s Chip Scale Atomic Clock*, Microsemi Corporation, Aliso Viejo, CA, USA, 2015.

[28] B. J. Bloom *et al.*, "An optical lattice clock with accuracy and stability at the 10^-18 level," *Nature*, vol. 506, no. 7486, pp. 71–75, 2014.

[29] R. Lutwak, "Principles of atomic clocks," in *Proc. IEEE Int. Freq. Control Symp.*, San Francisco, CA, USA, 2011, pp. 1–141.

[30] R. Wynands and S. Weyers, "Atomic fountain clocks," *Metrologia*, vol. 42, no. 3, pp. S64–S79, Jun. 2005.

[31] F. Levi *et al.*, "Cryogenic fountain development at NIST and INRIM: Preliminary characterization," *IEEE Trans. Ultrason., Ferroelect., Freq. Control*, vol. 57, no. 3, pp. 600–605, Mar. 2010.

[32] S. Knappe *et al.*, "A microfabricated atomic clock," *Appl. Phys. Lett.*, vol. 85, no. 9, pp. 1460–1462, 2004.

[33] C. Wang *et al.*, "Chip-Scale molecular clock," *IEEE J. Solid-State Circuits*, vol. 54, no. 4, pp. 914–926, Apr. 2019.

[34] R. Han *et al.*, "Filling the gap: Silicon terahertz integrated circuits offer our best bet," *IEEE Microw. Mag.*, vol. 20, no. 4, pp. 80–93, Apr. 2019.

[35] P. Hillger, J. Grzyb, R. Jain, and U. R. Pfeiffer, "Terahertz imaging and sensing applications with silicon-based technologies," *IEEE Trans. THz Sci. Technol.*, vol. 9, no. 1, pp. 1–19, Jan. 2019.

[36] K. Sengupta, T. Nagatsuma, and D. M. Mittleman, "Terahertz integrated electronic and hybrid electronicphotonic systems," *Nature Electron.*, vol. 1, no. 12, pp. 622–635, 2018.

[37] R. Han *et al.*, "A 320 GHz phase-locked transmitter with 3.3 mW radiated power and 22.5 dBm EIRP for heterodyne THz imaging systems," in *Proc. Int. Solid-State Circuit Conf.*, San Francisco, CA, USA, 2015, pp. 1–3.

[38] Z. Hu, M. Kaynak, and R. Han, "High-power radiation at 1-THz in silicon: A fully scalable array using a multi-functional radiating mesh structure," *IEEE J. Solid-State Circuits*, vol. 53, no. 5, pp. 1313–1327, May 2018.

[39] W. Knap *et al.*, "Plasma wave detection of sub-terahertz and terahertz radiation by silicon field-effect transistors," *Appl. Phys. Lett.*, vol. 85, no. 4, pp. 675–677, 2004.

[40] H. Sherry *et al.*, "A 1kpixel CMOS camera chip for 25fps real-time terahertz imaging applications," in *Proc. IEEE Int. Solid-State Circuits Conf.*, 2012, pp. 252–254.

[41] R. Han *et al.*, "A 280-GHz Schottky diode detector in 130-nm digital CMOS," *IEEE J. Solid-State Circuits*, vol. 46, no. 11, pp. 2602–2612, Nov. 2011.

[42] R. Han *et al.*, "280 GHz and 860 GHz image sensors using Schottky-barrier diodes in 0.13 um digital CMOS," in *Proc. Int. Solid-State Circuits Conf.*, San Francisco, CA, USA, 2012, pp. 254–257.

[43] C. Jiang *et al.*, "A 320 GHz subharmonic-mixing coherent imager in 0.13 um SiGe BiCMOS," in *Proc. Int. Solid-State Circuits Conf.*, San Francisco, CA, USA, 2016, pp. 432–434.

[44] Z. Hu, C. Wang, and R. Han, "A 32-Unit 240-GHz heterodyne receiver array in 65-nm CMOS with array-wide phase locking," *IEEE J. Solid-State Circuits*, vol. 54, no. 5, pp. 1216–1227, May 2019.

[45] P. Y. Chiang, Z. Wang, O. Momeni, and P. Heydari, "A 300 GHz frequency synthesizer with 7.9% locking range in 90 nm SiGe BiCMOS," in *Proc. IEEE Int. Solid-State Circuits Conf.*, San Francisco, CA, USA, 2014, pp. 260–261.

[46] Y. Zhao *et al.*, "An integrated 0.56 THz frequency synthesizer with 21 GHz locking range and −74 dBc/Hz phase noise at 1 MHz offset in 65 nm CMOS," in *Proc. IEEE Int. Solid-State Circuits Conf.*, San Francisco, CA, USA, 2016, pp. 36–37.

[47] Jet Propulsion Laboratory, "Molecular spectroscopy catalog," Jet Propulsion Laboratory, Pasadena, CA, USA. [Online]. Available: https://spec.jpl.nasa.gov/. Accessed on: Jun. 4, 2019.

[48] HITRAN: High-resolution transmission molecular absorption database. [Online]. Available: http://hitran.org/. Accessed on: Jun. 4, 2019.

[49] A. Mann, "Amazingly precise optical atomic clocks are more than timekeepers," *Proc. Nat. Acad. Sci.*, vol. 115, no. 29, pp. 7449–7451, 2018.

[50] D. J. Jones *et al.*, "Carrier-envelope phase control of femtosecond mode-locked lasers and direct optical frequency synthesis," *Science*, vol. 288, pp. 635–639, 2000.

[51] S. L. Coy, "Speed dependence of microwave rotational relaxation rates," *J. Chem. Phys.*, vol. 73, no. 11, 1980, Art. no. 5531.

[52] M. A. Koshelev and M. Y. Tretyakov, "Collisional broadening and shifting of OCS rotational spectrum lines," *J. Quantitative Spectrosc. Radiative Transfer*, vol. 110, no. 1/2, pp. 118–128, 2009.

[53] M. A. Koshelev, M. Y. Tretyakov, F. Rohart, and J. P. Bouanich, "Speed dependence of collisional relaxation in ground vibrational state of OCS: Rotational behaviour," *J. Chem. Phys.*, vol. 136, no. 12, pp. 124316-1–124316-10, 2012.

[54] H. Takahashi *et al.*, "Hermetic sealing technique for F-band waveguides and packages," in *Proc. 41st Eur. Microw. Conf.*, Manchester, U.K., 2011, pp. 269–272.

[55] *Road Vehicles—Component Test Methods for Electrical Disturbances From Narrowband Radiated Electromagnetic Energy—Part 8: Immunity to Magnetic Fields*, ISO-11452-8, International Organization for Standardization (ISO), Geneva, Switzerland, 2015.

[56] W. H. Flygare, W. Hüttner, R. L. Shoemaker, and P. D. Foster, "Magnetic susceptibility anisotropy, molecular quadrupole moment, and the sign of the electric dipole moment in OCS," *J. Chem. Phys.*, vol. 50, no. 4, pp. 1714–1719, 1969.

[57] J. R. Eshbach and M. W. P. Strandberg, "Rotational magnetic moments of sigma molecules," *Physical Rev.*, vol. 85, no. 1, pp. 24–34, 1952.

[58] J. T. Cox and W. Gordy, "Zeeman effect of some linear and symmetric-top molecules," *Physical Rev.*, vol. 101, no. 4, pp. 1298–1304, 1956.

[59] M.-K. Lo and W. H. Flygare, "Rotational magnetic moment of OCS," *Physical Rev.*, vol. 154, no. 1, pp. 93–94, 1967.

[60] D. H. Sutter and W. H. Flygare, "The molecular zeeman effect," in *Topics Current Chemistry: Bonding Structure*. Berlin, Germany: Springer-Verlag, 1976, pp. 89–196.

[61] S. V. Berdyugina and S. K. Solanki, "The molecular Zeeman effect and diagnostics of solar and stellar magnetic fields: I. Theoretical spectral patterns in the Zeeman regime," *Astron. Astrophys.*, vol. 385, pp. 701–715, 2002.

[62] C. Wang, X. Yi, M. Kim, Y. Zhang, and R. Han, "A CMOS molecular clock probing 231.061-GHz rotational line of OCS with sub-ppb long-term stability and 66-mW DC power," in *Proc. Symp. VLSI Technol. Circuits*, Honolulu, HI, USA, 2018, pp. 113–114.

[63] H.-J. Song, "Packages for terahertz electronics," *Proc. IEEE*, vol. 105, no. 6, pp. 1121–1138, 2017.

[64] H. Lee *et al.*, "Intel 22 nm FinFET (22FFL) process technology for RF and mmWave applications and circuit design optimization for FinFET technology," in *Proc. IEEE Int. Electron Devices Meeting*, San Francisco, CA, USA, 2018, pp. 316–319.

[65] B. Heinemann *et al.*, "SiGe HBT with fT/fmax of 505 GHz/720 GHz," in *Proc. IEEE Int. Electron Device Meeting*, San Francisco, CA, USA, 2016, pp. 51–54.

[66] B. Beuerle, J. Campion, U. Shah, and J. Oberhammer, "A very low loss 220–325 GHz silicon micromachined waveguide technology," *IEEE Trans. THz. Sci. Technol.*, vol. 8, no. 2, pp. 248–250, Mar. 2018.

**Mina Kim** (S'15) received the B.S. and M.S. degrees in electrical engineering from the Ulsan National Institute of Science and Technology, Ulsan, South Korea, in 2013 and 2016, respectively. She is currently working toward the Ph.D. degree in electrical engineering and computer science with the Massachusetts Institute of Technology, Cambridge, MA, USA.

Her research interests include clock generation and millimeter/terahertz-wave integrated circuit design.

Dr. Kim was a recipient of the MIT EECS Graduate Alumni Fellowship, and the Kwanjeong Scholarship for the Graduate Study in 2017.

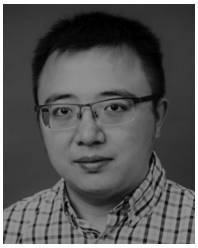

**Cheng Wang** (S'12) received the B.E. degree in engineering physics from Tsinghua University, Beijing, China, in 2008, the M.S. degree in radio physics from the China Academy of Engineering Physics, Mianyang, China, in 2011, and the M.S. degree in electrical engineering and computer science (EECS) from the Massachusetts Institute of Technology (MIT), Cambridge, MA, USA, in 2018. He is currently working toward the Ph.D. degree in electrical engineering and computer science with the Department of Electrical Engineering and Computer Science, MIT.

He joined the Institute of Electronic Engineering, Mianyang, China as an Assistant Research Fellow from 2011 to 2015. His research interests include millimeter/terahertz-wave gas spectroscopy, high-precision clock generation, wireless communication, and automotive radar.

Dr. Wang was the recipient of the Analog Device, Inc., Outstanding Student Designer Award in 2016. In 2017, he was the recipient of the IEEE Microwave Theory and Techniques Society Boston Chapter Scholarship.

**Zhi Hu** (S'15) received the B.S. degree in microelectronics from Fudan University, Shanghai, China, in 2015, and the M.S. degree in electrical engineering from the Massachusetts Institute of Technology, Cambridge, MA, USA, in 2017. He is currently working toward the Ph.D. degree in electrical engineering with the Massachusetts Institute of Technology, Cambridge, MA, USA.

In the summer of 2016, he was a Visiting Researcher with IHP Microelectronics, Frankfurt, Germany. His current research interests include integrated circuit design at terahertz and millimeter-wave frequency band, with a special focus on improving the performance of on-chip terahertz power sources and receivers using multi-functional and large-scale dense array structures for imaging and sensing applications.

Dr. Hu was the recipient of the Best Student Paper Award (2nd place) of the 2017 IEEE Radio-Frequency Integrated Circuits Symposium (RFIC). He was a recipient of the KLA-Tencor Scholarship in 2014 and the SCSK Scholarship in 2013. He is a member of the IEEE Solid-State Circuits Society and the IEEE Microwave Theory and Techniques Society.

**Ruonan Han** (S'10–M'14) received the B.Sc. degree in microelectronics from Fudan University, Shanghai, China, in 2007, the M.Sc. degree in electrical engineering from the University of Florida, Gainesville, FL, USA, in 2009, and the Ph.D. degree in electrical and computer engineering from Cornell University, Ithaca, NY, USA, in 2014.

In 2012, he was an Intern with Rambus Inc., Sunnyvale, CA, USA. He is currently an Associate Professor with the Department of Electrical Engineering and Computer Science, Massachusetts Institute of Technology, Cambridge, MA, USA. His current research interests include microelectronic circuits and systems operating at millimeter-wave and terahertz frequencies.

Dr. Han is a member of the IEEE Solid-State Circuits Society and the IEEE Microwave Theory and Techniques Society. He is an Associate Editor for the IEEE TRANSACTIONS ON VERY-LARGE-SCALE INTEGRATION SYSTEM and also serves on the Technical Program Committee (TPC) of the IEEE RFIC Symposium and the Steering Committee of 2019 IEEE International Microwave Symposium. He was the recipient of the Cornell ECE Directors Ph.D. Thesis Research Award, Cornell ECE Innovation Award, and two Best Student Paper Awards of the IEEE Radio-Frequency Integrated Circuits Symposium (2012 and 2017). He was also the recipient of the IEEE Microwave Theory and Technique Society Graduate Fellowship Award, and the IEEE Solid-State Circuits Society Predoctoral Achievement Award. He is the winner of the Intel Outstanding Researcher Award (2019) and the National Science Foundation (NSF) CAREER Award (2017).